Supplementary materials:

A case study of the highly time-resolved evolution of aerosol chemical and optical properties in urban Shanghai, China

Yuanlong Huang[a], Ling Li[a], Jingyan Li[a], Xinning Wang[a], Hong Chen[a], Jianmin Chen[a,b], Xin Yang[a,b]*, Deborah S. Gross[c], Hongli Wang[d], Liping Qiao[d], Changhong Chen[d]

[a]Shanghai Key Laboratory of Atmospheric Particle Pollution and Prevention, Department of Environmental Science and Engineering, Fudan University, Shanghai 200433, China
[b]Research Institute for Changing Global Environment, Fudan University, Shanghai 200433, China
[c]Department of Chemistry, Carleton College, Northfield, MN 5507,USA
[d]Shanghai Academy of Environmental Sciences, Shanghai 200233, China

Correspondence to: Xin Yang (yangxin@fudan.edu.cn)

1. Size distributions of different particle types

In China, most of the biomass burning particles come from crop residue burning. In this work, based on our laboratory research on the particles emitted from rice straw, wheat straw and corn stalk burning (paper in preparation), we set several criteria for identifying biomass burning particles: 1) There should be K-clusters such as $^{113}K_2Cl^+$ and $^{213}K_3SO_4^+$ in the positive MS. 2) $^{26}CN^-$ should occur in the negative MS. 3) No $^7Li^+$ should be observed (Liu et al., 2003; Spencer et al., 2008; Furutani et al., 2011). Biomass burning particles have been shown to have significant signals at *m*/*z* +23 (Na^+) and +39 ($K^+/C_3H_3^+$) in the positive spectra and *m*/*z* -26 (CN^-) in the negative spectra. As shown in Fig. 2a, a 0.12 μm difference (0.28 versus 0.40 μm) was observed between the maxima of the size distributions of fresh and aged biomass burning groups, which is consistent with previous studies(Reid et al., 2005). Note that in the larger size range (>0.8 μm), aged biomass burning aerosols still make up 15% of particles observed with the ATOFMS.

Characterized by peaks of *m*/*z* +18 (NH_4^+), +27 ($C_2H_3^+$), +39 ($K^+/C_3H_3^+$) and +43 ($C_2H_3O^+$) in the positive spectra, organic carbon (OC) particles account for 26.6% of all particles. A peak gap (about 0.1 μm) exists between the maximum of the size distribution of fresh and aged OC types, with the peak of fresh OC type at a smaller diameter of 0.48 μm. Elemental Carbon/Organic Carbon (ECOC) particles have mass spectra containing a mixture of carbon clusters (C_n^+) and major OC peaks, and account for 8.7% of particles observed. Both fresh and aged ECOC groups have secondary markers of (NH_4^+) and ($C_2H_3O^+$). The size distribution of ECOC is bimodal. For the fresh ECOC type, the mode with higher number concentration is centered around 0.28 μm and the other is around 0.64 μm. It is the same situation for the aged type, however, the larger size mode is higher compared to the fresh (Fig.2, 0.32 and 0.68 μm, respectively). The mass spectral pattern of the ammonium group has a significant ion peak of *m*/*z* +18 (NH_4^+) in the positive spectra. Other peaks include OC fragments of *m*/*z* +27 ($C_2H_3^+$), +39 ($K^+/C_3H_3^+$), +43 ($C_2H_3O^+$) in positive spectra and -46 (NO_2^-), -62 (NO_3^-), -97 (HSO_4^-), and -125 ($H(NO_3)_2^-$) in negative spectra. The size distribution of the number fraction of the ammonium type increases with the diameter.

Other groups including EC, dust, metal-containing, and Na-K-rich groups are named after their mass spectral features, and together they account for 15.9% of all observed particles. EC particles are characterized by clusters of carbon ($C_n^{+/-}$), mainly distributed in the small size range (making up ~50% of all particle groups with diameter smaller than 0.24 μm). The particles with signals from *m*/*z* +40 (Ca^+), +57 ($CaOH^+$), -60 (SiO_2^-), -76 (SiO_3^-), and -79 (PO_3^-) were classified as dust. They are also mixed with Na, K, nitrate and sulfate. Most dust particles have diameters of 0.8 - 1.2 μm. Particles containing typical metal elements, e.g. Na, Mg, Al, K, V, Mn, Fe, and Pb, combine to make up the metal-containing group. The Na-K-rich type has strong intensities of Na and K in the positive spectra. Metal-containing and Na-K-rich particles all have nitrate and the the nitrate cluster in the negative spectra. Most particles in these two groups have diameters larger than 0.6 μm.

Metal-containing particles consist of several sub-groups including Fe-, Na-Al-K-Mn-, V- and Pb-containing particles, accounting for 4.3%, 2.0%, 0.7% and 1.2% of total particles, respectively. The Fe-containing particles can be further divided into three sub-types as well (Na-K-Fe-, 0.9%; Fe-S-N-, 1.7%; Fe-N-, 1.7%), according to the mass spectral patterns and temporal variations. Pb- and Fe-S-N-containing particles had similar temporal variations in number fraction (both having peaks during Period 2), indicating their sources were from the northwest of Shanghai. V-containing particles occurred only when the wind blew from the east suggesting ship emissions as their source (Ault et al., 2010). Fe-N- and Na-Al-K-Mn-containing particles had a nearly constant number fraction, indicating regional sources. Na-K-Fe-containing particles only occurred in Oct 13 with two spikes at around 11:00 and 16:00, possibly originating from a local source.

2. Discussion of sulfate-, nitrate-, and ammonium- containing particle fractions

Fig. S5 shows the size distributions of the number fraction of sulfate-, nitrate- and ammonium- containing particles sampled with the ATOFMS in the three time periods. The particles were filtered by the relative intensity of each marker using a threshold (relative peak areas greater than 0.1, 0.1, and 0.05, respectively). Note that all particles containing peaks due to ammonium are included here, even if they are assigned to other particle types. Sulfate particles were typically found in the size range of 0.4 - 0.6 μm (about 80%). The increased sulfate in Period 1 likely results from the high number fraction of EC particles, as discussed in the main document. The number fraction of nitrate- containing particles stayed nearly constant at around 80% for particles with size larger than 0.4 μm. This indicates that about 60-80% of particles incorporated more nitrite as they grew. The number fraction of ammonium-containing particles also increased as the diameter grew, and the maximum number fraction got as high as 55% around 1.2 μm in Period 2.

The size distribution trends of sulfate, nitrate, and ammonium were nearly the same in the three time periods. However, the nitrate- containing number fraction was almost 20% larger in Period 2 than in Periods 1 and 3 for particles larger than 0.4 μm. In addition, ammonium- and sulfate- containing number fractions exceeded nearly 30% and 20% in the size range of 0.8 - 1.2 μm. Periods 1 and 3 shared fairly similar size distributions of number fraction in the three periods. The shift of number fraction between different time periods could also be due to the influence of regional transport on local aerosol chemical properties. The higher fraction of nitrate and ammonium in Period 2 supports the suggestion of an input of NO_x and ammonia. Ammonia prefers partitioning from the gas phase to the particle phase when RH is high. High RH during

Period 2 (average RH ~83%, see Fig. S1) promoted the partitioning of ammonia into the particles. The enhancement of particulate ammonium attracts more acid into the particle phase. To neutralize ammonium, sulfuric acid first gets exhausted. Then more nitrate acid partitions into the particle to neutralize the excess ammonium. So in the second period both the sulfate- and nitrate-containing particle number fraction was greater than in the other two periods, especially in the large size range.

References:

Ault, A. P., Gaston, C. J., Wang, Y., Dominguez, G., Thiemens, M. H., and Prather, K. A.: Characterization of the Single Particle Mixing State of Individual Ship Plume Events Measured at the Port of Los Angeles, Environ. Sci. Technol., 44, 1954-1961, doi:10.1021/es902985h, 2010.

Furutani, H., Jung, J., Miura, K., Takami, A., Kato, S., Kajii, Y., and Uematsu, M.: Single-particle chemical characterization and source apportionment of iron-containing atmospheric aerosols in Asian outflow, J. Geophys. Res., 116, D18204, doi:10.1029/2011jd015867, 2011.

Liu, D. Y., Wenzel, R. J., and Prather, K. A.: Aerosol time-of-flight mass spectrometry during the Atlanta Supersite Experiment: 1. Measurements, J. Geophys. Res.-Atmos., 108, 8426, doi:10.1029/2001jd001562, 2003.

Reid, J. S., Koppmann, R., Eck, T. F., and Eleuterio, D. P.: A review of biomass burning emissions part II: intensive physical properties of biomass burning particles, Atmos. Chem. Phys., 5, 799-825, doi:10.5194/acp-5-799-2005, 2005.

Spencer, M. T., Holecek, J. C., Corrigan, C. E., Ramanathan, V., and Prather, K. A.: Size-resolved chemical composition of aerosol particles during a monsoonal transition period over the Indian Ocean, J. Geophys. Res.-Atmos., 113, D16305, doi:10.1029/2007jd008657, 2008.

Spencer, M. T., and Prather, K. A.: Using ATOFMS to determine OC/EC mass fractions in particles, Aerosol Sci. Tech., 40, 585-594, doi:10.1080/02786820600729138, 2006.

Table S1. Results of linear regression of the scattering, absorption, and extinction coefficients versus PM_1 mass loading in the four sub-periods.

Time Period	Scattering		Absorption		Extinction	
	Slope (m^2 g^{-1})	R^2	Slope (m^2 g^{-1})	R^2	Slope (m^2 g^{-1})	R^2
Period 1a	1.41±0.17	0.86	0.63±0.08	0.85	2.04±0.21	0.90
Period 2a	4.31±0.34	0.93	0.86±0.05	0.95	5.17±0.38	0.94
Period 2b	1.54±0.15	0.88	0.76±0.09	0.82	2.29±0.22	0.88
Period 3a	2.80±0.51	0.77	2.07±0.22	0.91	4.87±0.53	0.93

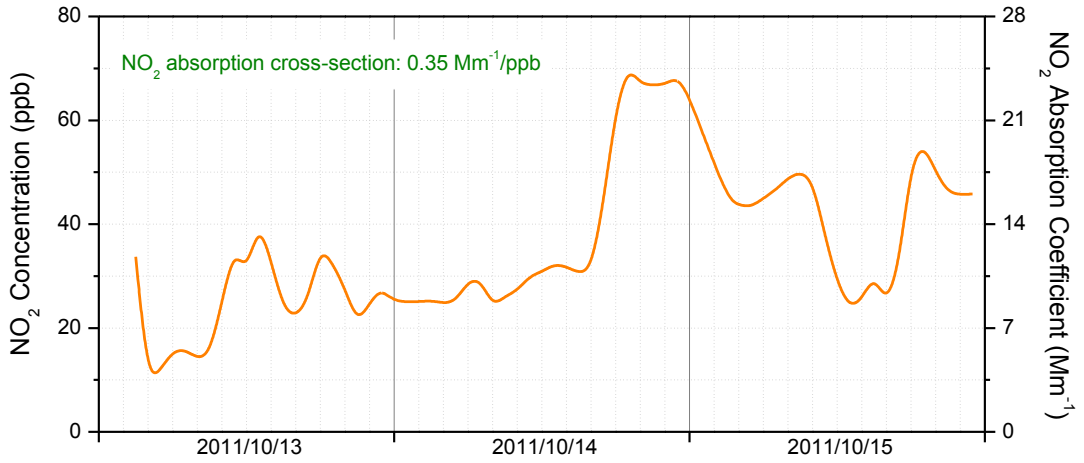

Figure S1. Temporal variation of NO_2 concentration and absorption coefficient over Oct 13-15, 2011 in one-hour resolution.

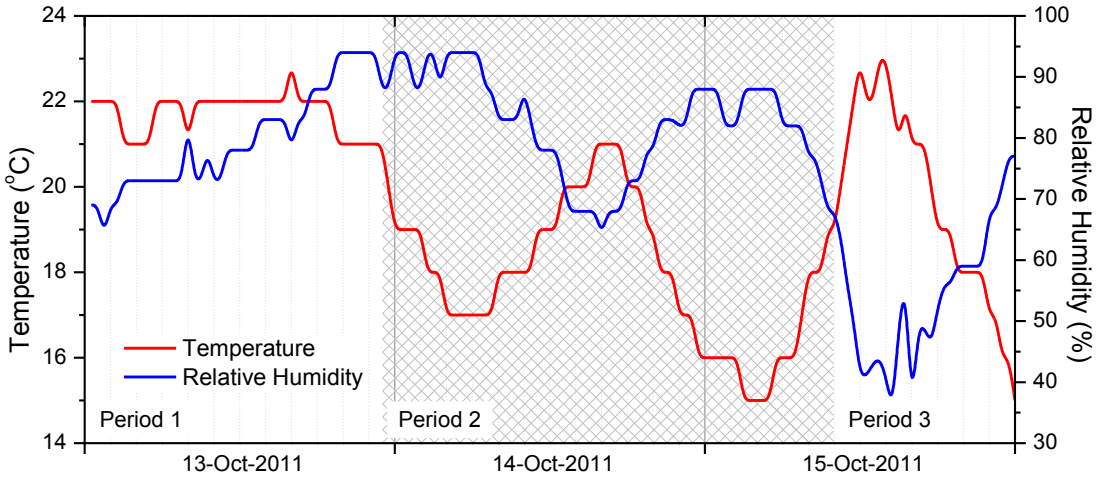

Figure S2. Temporal variation of temperature and RH over Oct 13-15, 2011 with 30-minute resolution.

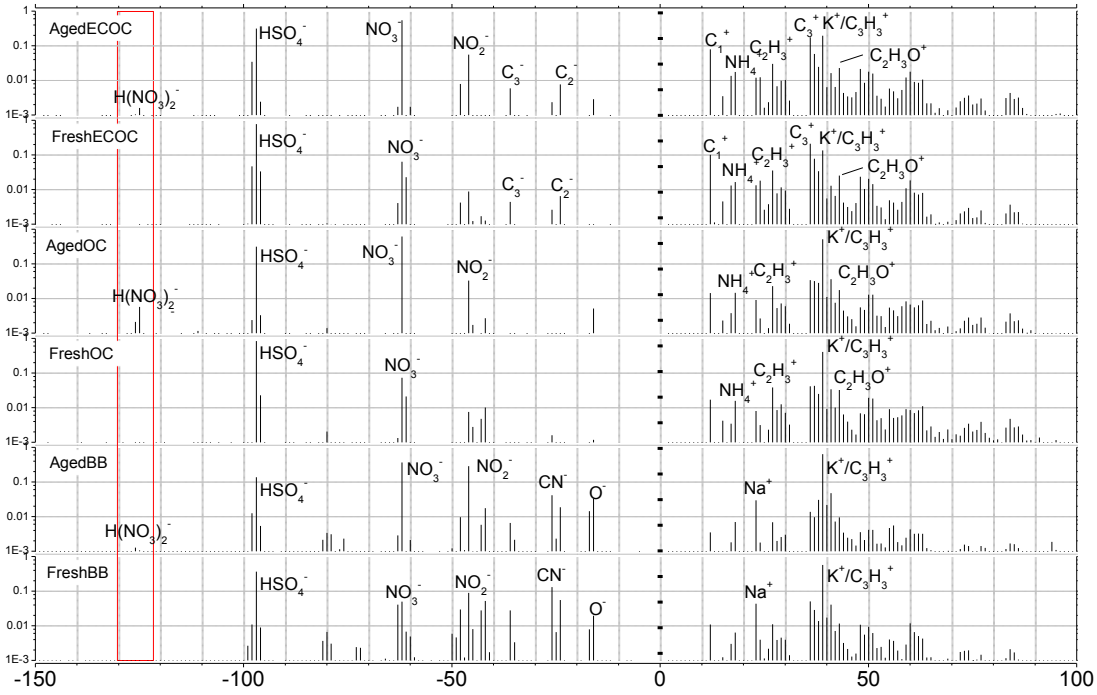

Figure S3. ATOFMS spectra for fresh and aged biomass burning (BB), organic carbon (OC) and elemental/organic carbon (ECOC) particle types. The red box highlights the nitrate cluster ion $H(NO_3)_2^-$, a marker for aging.

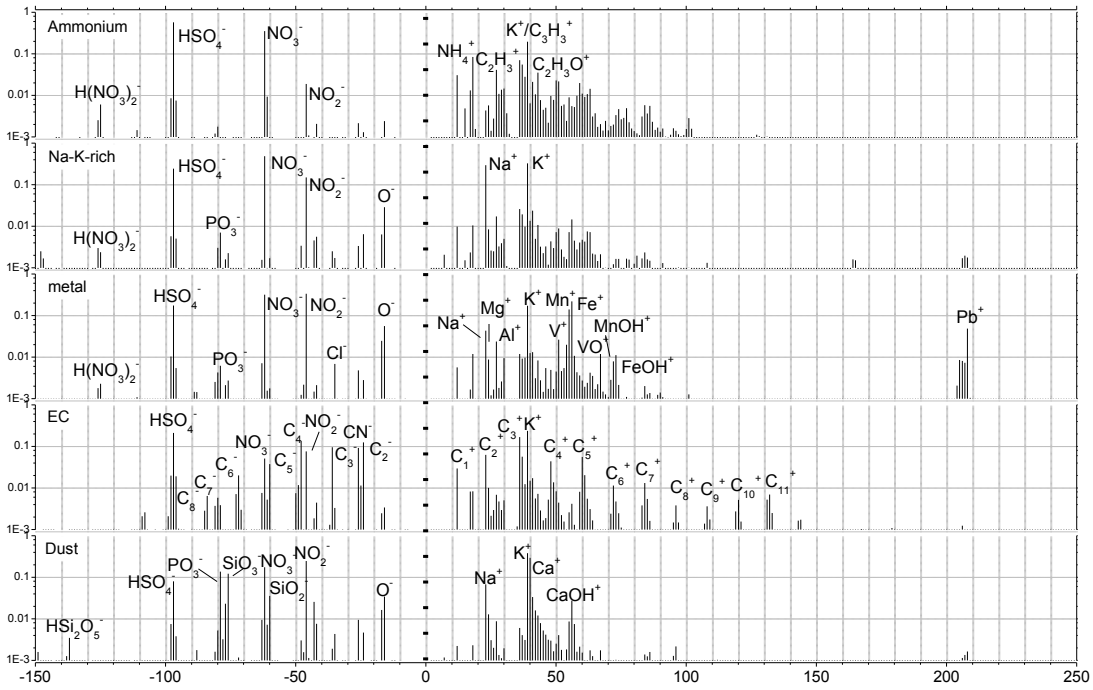

Figure S4. ATOFMS spectra for ammonium, Na-K-rich, metal, elemental carbon (EC) and dust-containing particle types.

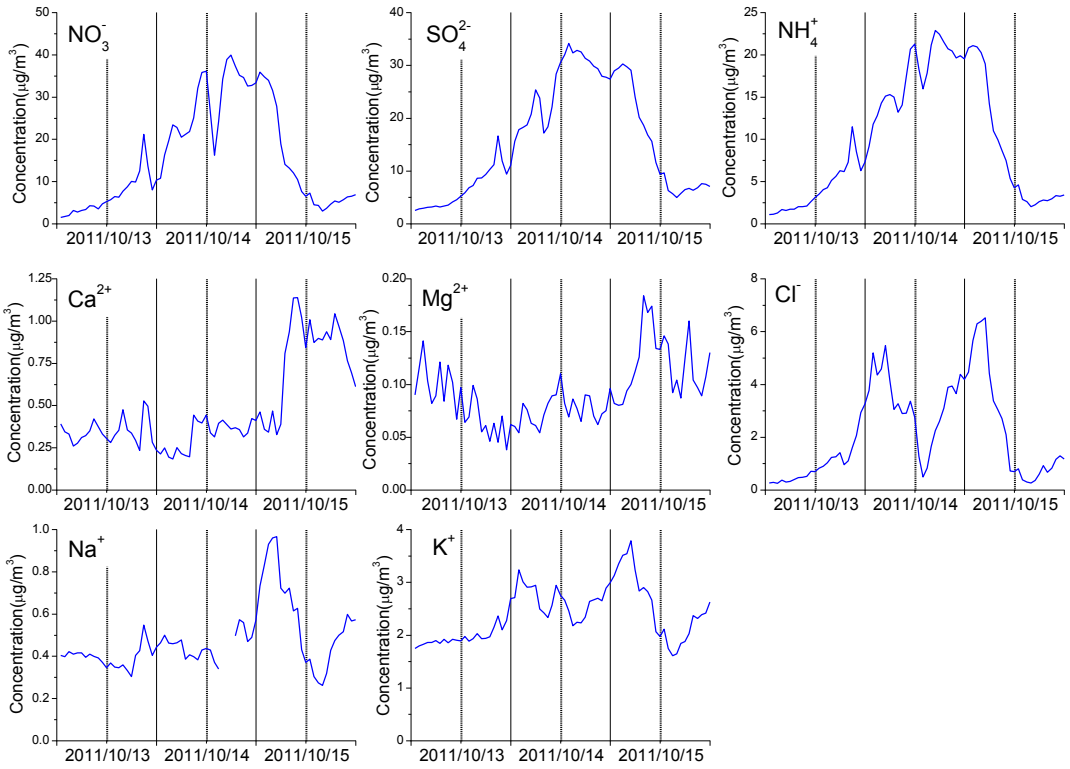

Figure S5. Temporal profiles of eight water-soluble ion mass concentrations measured by MARGA.

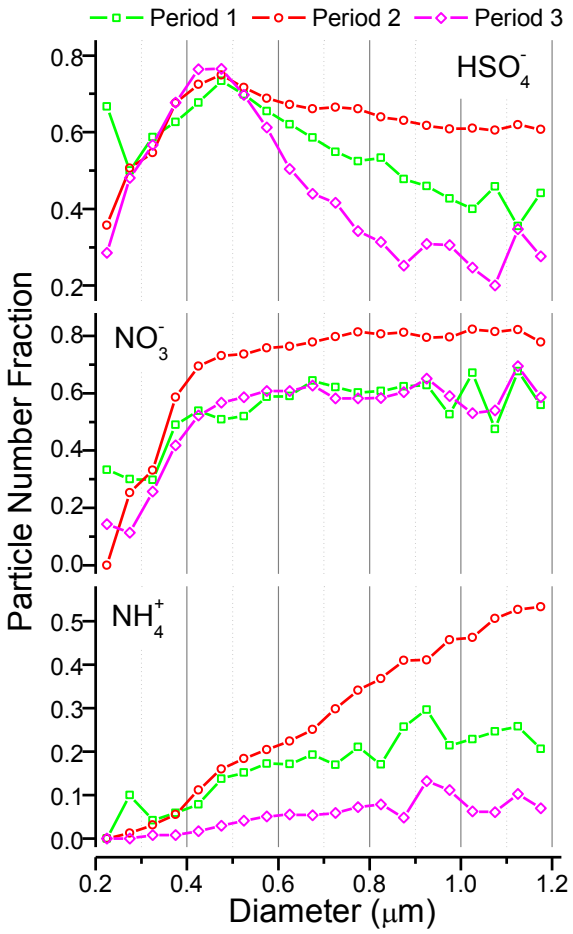

Figure S6. Size distributions of number fractions of particles sampled with the ATOFMS containing HSO_4^- (*m*/*z* -97), NO_3^- (*m*/*z* -62) and NH_4^+ (*m*/*z* +18) in the three time-periods.

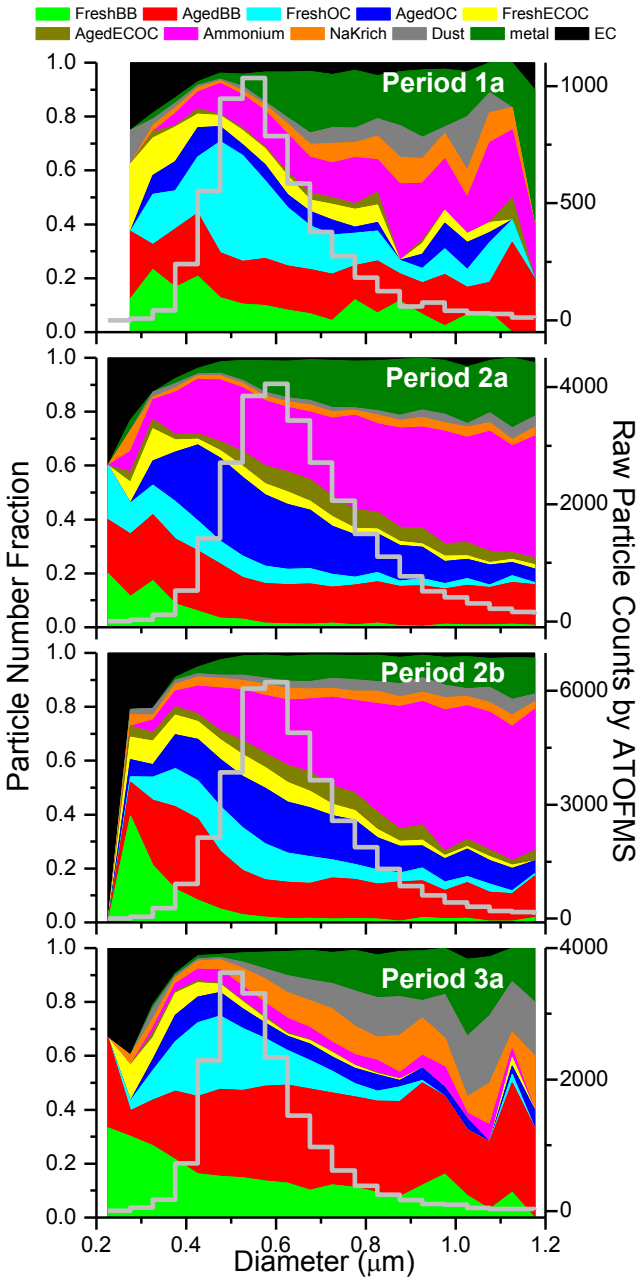

Figure S7. Chemically resolved size distributions of different particle type number fractions and raw particle counts by ATOFMS in the four sub-periods.

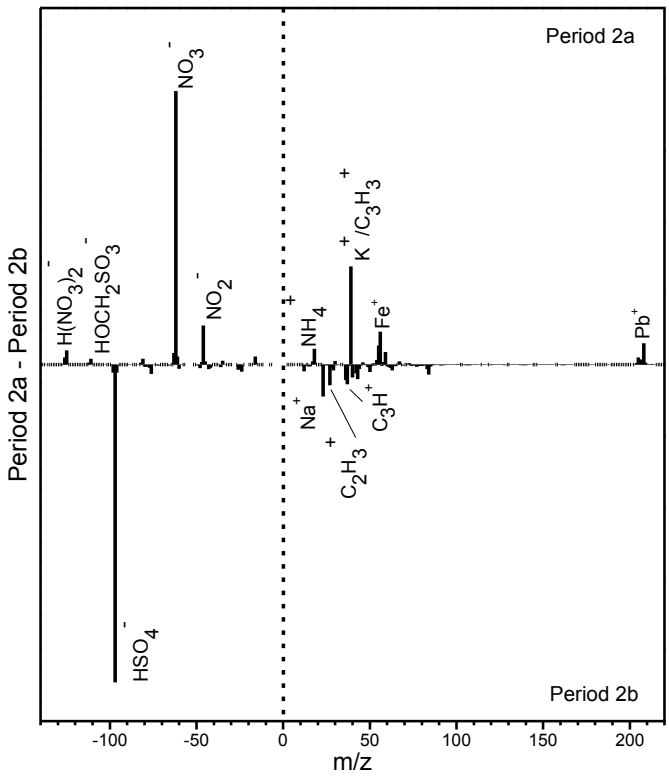

Figure S8. Difference of the average mass spectra (relative peak area) of particles in Period 2a and Period 2b.

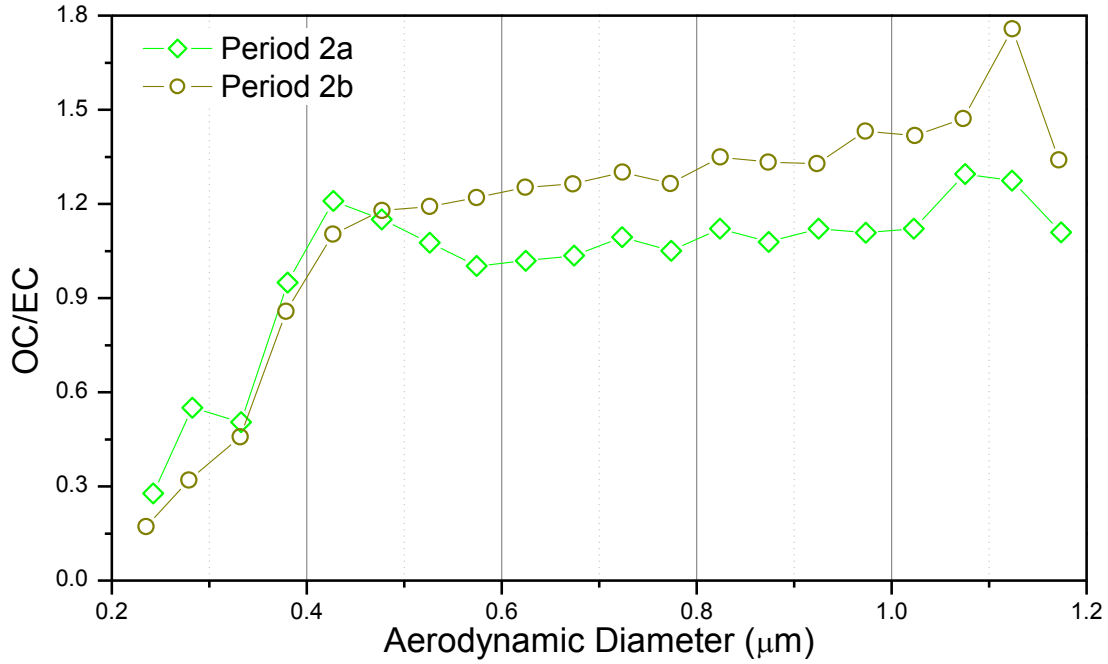

Figure S9. Sized resolved distributions of the OC/EC ion ratio (Spencer and Prather, 2006) in carbonaceous particles in Period 2a and Period 2b.